

Non-Gaussian Signal Statistics in Ocean SAR Imagery

Torbjørn Eltoft, *Associate Member, IEEE*, and Kjell A. Høgda

Abstract—In this paper, we have studied the significance of non-Gaussian signal statistics in some synthetic aperture radar (SAR) images of the ocean surface. The study consisted of calculating the amplitude histogram of the returned echoes from the images and comparing these with the Rayleigh- and K_v -distributions, corresponding to the Gaussian and non-Gaussian statistics, respectively. The images used were some C-band SAR data from the Canadian airborne SAR collected during the NORCSEX'88 campaign and some ERS-1 data collected during the NORCSEX'91 campaign. The analysis of the NORCSEX'88 data included studies of the dependency of the signal statistics on incidence angle and meteorological and imaging conditions. It was found, specifically at small incidence angles, that there was a significant deviation from Gaussian statistics. It was also found that when the wind was blowing against the waves, the deviation from Gaussian statistics was more pronounced than when the wind was blowing in the same direction as the waves were propagating. The study also showed a correlation between the signal statistics and the width of the SAR image spectra. At low incidence angles, this agrees with the interpretation that non-Gaussian statistics may be related to strong widebanded scattering events. However, since non-Gaussian statistics also were observed at incidence angles as high as 50° , it is evident that the modulation of the scattering cross section by the long waves is also an important factor. In addition, the analysis of the ERS-1 data showed that to account for the width of the SAR image spectra, an azimuth smearing term, due to short scene coherence time, had to be included. This was in the present work done by modeling the *short-coherence-time-smearing* as a Gaussian low-pass filter. By this procedure, we were able to obtain realistic estimates for the average scene coherence time of the SAR scenes.

Index Terms—Azimuth smearing, K -distribution, microwave radar backscatter, non-Gaussian statistics, scene coherence time, signal statistics, synthetic aperture radar (SAR) imaging.

I. INTRODUCTION

OVER THE LAST couple of decades there has been considerable interest in the imaging of the ocean surface by synthetic aperture radars (SAR's). Through the years, several theories for the relationship between the SAR image spectrum and the actual ocean-surface wave spectrum have been developed (e.g., [1]–[3]). This problem seems to have come closer to a solution by the Hasselmann transform [4], [5], which gives a closed-form expression for the nonlinear velocity-bunching effect. There is, however, still much re-

search that needs to be done to completely understand the scattering mechanisms responsible for the microwave return and the tilt and hydrodynamic modulation mechanisms, by which the intensity of the backscattered signals are modulated by ocean waves. It seems to be widely accepted that Bragg scattering is the basic scattering mechanism producing the return at incidence angles between 20° and 70° and that specular point reflections are limited to incidence angles less than 20° (e.g., [6]). However, there are some indications that specular-point reflections may play an important role in SAR imaging of steep, wind-driven waves and more complex ocean scenes involving internal waves and ocean fronts, even at incidence angles greater than 20° . Azimuth streaks, i.e., discrete features of high intensities streaked in the azimuth direction, which are believed to be associated with breaking waves, have been observed in some SEASAT SAR images of high-wind areas [7] and in some airborne SAR images of the British Channel [8].

In the present paper, we investigate the statistics of some airborne and spaceborne C-band SAR images. The data sets are from the NORCSEX'88 and NORCSEX'91 experiments. The analysis is motivated from the hypothesis that specular-point reflections will render strong discrete broadbanded echoes, which will result in non-Gaussian signal statistics. Scenes dominated by Bragg scattering, on the other hand, are expected to provide signals with Gaussian statistics [9]. In the literature, there are many reports on observations of sea-clutter statistics that deviate from Gaussian statistics, and in some of these papers, the observations have been found to be directly related to the scattering mechanism producing the echoes (e.g., [10] and [11]).

The objectives of the present study are to investigate the dependency of the signal statistics on imaging and meteorological conditions and to find out if there is any correlation between the azimuth width of the SAR image spectra and deviation from Gaussian signal statistics. We do this by comparing the amplitude distribution of the returned signals and those corresponding to Gaussian and non-Gaussian signals, respectively. Gaussian signals are known to have Rayleigh-distributed amplitudes. We have found it feasible to use the K -model to describe the amplitude statistics of non-Gaussian signals. The K -distributions have been found to have a wide area of applicability, including microwave return from the ocean surface [8], [11]–[13]. They are mathematically formulated by modified Bessel functions in such a way that, as the order of the Bessel function gets large, the shape of the probability-density function approximates that of the

Manuscript received June 27, 1996; revised June 2, 1997.

T. Eltoft is with the Institute of Mathematical and Physical Sciences, University of Tromsø, N-9037 Tromsø, Norway (e-mail: torbjorn.eltoft@phys.uit.no).

K. A. Høgda is with NORUT Information Technology Ltd., N-9005 Tromsø, Norway.

Publisher Item Identifier S 0196-2892(98)00553-1.

Rayleigh distribution. Thus, the order parameter can be used as an indicator of the degree of non-Gaussian signal statistics. However, we note that in [14] Gotwols and Thompson have shown that, at least at intermediate incidence angles, the sea echoes can be better described by another compound distribution, which they develop from a physical scattering model.

This paper is organized as follows. Section II gives a short review of some theoretical preliminaries. Section III describes the data sets and analyzing methods. In Section IV, we present the results of the analysis of the NORCSEX'88 and NORCSEX'91 data sets, and in Section V, we include a discussion of the analysis and results. Finally, in Section VI we give our conclusions.

II. SOME THEORETICAL PRELIMINARIES

We include in this section some theory of the scattering of microwaves from the ocean surface and discuss how the scattering may influence on the amplitude statistics of the returned signals. Since one of the objectives of this work is to study the correlation between the signal statistics and the azimuth smearing in some SAR images, we also include a short discussion on some important aspects of the SAR imaging of moving scatterers with limited coherence time, with special emphasis on the impacts on the azimuth resolution of the images.

A. Scattering Theory

In the case of a planar surface, the backscattered electromagnetic field can be approximated by using the small perturbation method, which yields a backscattered field proportional to the spectral density of the surface roughness at wavenumber $\pm 2\kappa_H$, where κ_H is the horizontal projection of the radar wavenumber. This is the Bragg model. However, the ocean surface contains a broad range of roughness scales. The small-scale waves are subject to local tilting and advection by the large-scale ocean waves, and this mechanism has been attempted and accounted for in the so-called *composite model* [15]. In the composite scattering model, the ocean surface is divided into two length scales, i.e., $\eta(\mathbf{x}, t) = \eta_L(\mathbf{x}, t) + \eta_S(\mathbf{x}, t)$, where $\eta_L(\mathbf{x}, t)$ represents the long gravity waves and $\eta_S(\mathbf{x}, t)$ represents the short waves. $\eta_S(\mathbf{x}, t)$ is defined, such that $2\kappa_z\eta_S(\mathbf{x}, t) \ll 1$, where κ_z is the vertical component of the incident radar wavenumber. Using a two-scale representation of the sea surface, it was shown in [16] that the surface current can be expressed as

$$\begin{aligned} \mathbf{B}(\mathbf{R}_0, t) = & \frac{1}{2\pi i} \frac{e^{i\kappa R_0}}{R_0} \int G(\mathbf{x}) \\ & \exp[-2i\kappa_H \cdot \mathbf{x} - 2i\kappa_z\eta_L(\mathbf{x}, t) \\ & - 2i\kappa_H \cdot \mathbf{u}(\mathbf{x}, t)t] \\ & \times \left\{ [\kappa_z - \kappa_H \cdot \Delta\eta_L(\mathbf{x}, t)][1 - 2i\kappa_z\eta_S(\mathbf{x}, t)]\mathbf{B}_0 \right. \\ & \left. + 2\mathbf{B}_0 \cdot [\hat{\mathbf{z}} \times \Delta\eta_S(\mathbf{x}, t)] \frac{\kappa_H \times \kappa}{\kappa_z} \right\} d\mathbf{x}. \quad (1) \end{aligned}$$

In (1), $\kappa = (\kappa_H, \kappa_z)$ is the radar wavelength, \mathbf{B}_0 is the incident field, $G(\mathbf{x})$ is the antenna function, $\hat{\mathbf{z}}$ is a unit vector along the z -axis, and R_0 is the distance to the center of the antenna footprint. The term $\exp[-2i\kappa_H \cdot \mathbf{u}(\mathbf{x}, t)t]$ accounts for the horizontal motion of the long-scale surface, where $\mathbf{u}(\mathbf{x}, t)$ represents the horizontal large-scale velocity field. The expression in (1) is derived by an iteration of the surface-current integral equation retaining all terms through those that are linear in the surface slope, assuming the ocean surface to be a perfect conductor. This is similar to the procedure used in [17]. For further details on this time-dependent scattering model, we refer to [18] and [19]. We note that the expression in (1) reduces to the Bragg model when $\eta_L(\mathbf{x}, t) = 0$ and to specular-point scattering from a long-wave surface when $\eta_S(\mathbf{x}, t) = 0$ [16].

B. Signal Statistics

Since the sea surface is of a random nature, the backscattered signal is a random process that requires a statistical description. We derive the statistical distribution of the backscattered signal by formulating the complex envelope of the received signal from each resolution cell as a superposition of contributions from N -different scattering centers, i.e.,

$$\begin{aligned} s(\mathbf{r}, t) &= \sum_{i=1}^N a_i(\mathbf{r}, t) \exp[j\varphi_i(\mathbf{r}, t)] \\ &= A(\mathbf{r}, t) \exp[j\phi(\mathbf{r}, t)] \end{aligned} \quad (2)$$

where $a_i(\mathbf{r}, t)$ and $\varphi_i(\mathbf{r}, t)$ are amplitude and phase of the i th scattering center, respectively. $a_i(\mathbf{r}, t)$ governs the strength and angular distribution of the radiation, and $\varphi_i(\mathbf{r}, t)$ is dependent on the position of this element at time t , with respect to the observation point \mathbf{r} . By using the assumption of no phase correlation between the different scattering centers, it can be shown that the characteristic function of the received signal is

$$C(\Omega) = \left\{ \int_0^\infty p_a(a) J_0(a\Omega) da \right\}^N \quad (3)$$

where $p_a(a)$ is the probability-density function of the individual amplitudes a_i , and $J_0(x)$ is the zeroth-order Bessel function. From (3) we can derive two statistical models, as follows.

- 1) The number of scattering centers N is large, but non-fluctuating. In this case, the limit distribution as N approaches infinity becomes [11]

$$p_A(A) = \frac{A}{\sigma^2} \exp\left(-\frac{A^2}{2\sigma^2}\right) \quad (4)$$

where $\sigma^2 = \langle A^2 \rangle / 2$. This corresponds to Gaussian signal statistics.

- 2) The number of scattering centers is large and fluctuates according to a negative binomial distribution. This will yield K_ν -distributed amplitudes [20], where the

probability-density function is given by

$$p_A(A) = \frac{2b}{\Gamma(\nu)} \left(\frac{bA}{2} \right)^\nu K_{\nu-1}(bA), \quad \nu > 0 \quad (5)$$

where $b = 2(\nu/\langle A^2 \rangle)^{1/2}$:

- $\Gamma(\cdot)$ is the gamma function;
- $K_{\mu-1}$ is the modified Bessel function of the first kind and order $\mu - 1$.

It has been found (see e.g., [8], [12], and [20]) that when sea clutter tends to have non-Gaussian statistics, the backscattered signal amplitude can be well described by the K_ν model. The K_ν -distributions have some attractive properties; they are infinitely divisible, with respect to convolution, and they approach the Rayleigh distribution as $\nu \rightarrow \infty$. Their normalized intensity moments always lie between those of a Rayleigh distribution and those of a Log-Normal distribution. We also note that the K_ν distributions can be derived by averaging a compound probability model $p(A|\sigma_0)$ over a probability function $p(\sigma)$, assuming that $p(A|\sigma_0)$ is the Rayleigh distribution and that $p(\sigma_0)$ can be represented by a gamma distribution [21], [22]. σ_0 is the normalized radar cross section.

We return to (1) and assume that $\eta_L(\mathbf{x}, t)$ and $\eta_S(\mathbf{x}, t)$ are both zero-mean Gaussian processes, and that $E\{\eta_S(\mathbf{x}, t)\eta_L(\mathbf{x}, t)\} = 0$, where $E\{\cdot\}$ denotes ensemble averaging. For a high-resolution radar, having a resolution cell too small to contain enough independent scattering centers for the received field to be Gaussian, due to the central limit theorem, we can directly infer the following properties of the statistics of the return echoes.

- 1) For small values of $\kappa_z \eta_L(\mathbf{x}, t)$, the backscattered signal can be approximated as a linear function of $\eta_S(\mathbf{x}, t)$ and $\eta_L(\mathbf{x}, t)$ and the scattered signal will still be Gaussian.
- 2) For large values of $\kappa_z \eta_L(\mathbf{x}, t)$, the backscattered signal is a nonlinear function of $\eta_L(\mathbf{x}, t)$ and the signal statistics will in general become non-Gaussian.
- 3) When $\eta_S(\mathbf{x}, t) = 0$, (1) yields specular-point scattering from a long-wave surface and the backscattered signal will have non-Gaussian statistics.

Hence, from the above we conclude that, in the case of a high-resolution radar, non-Gaussian signal statistics may occur as a result of non-Bragg scattering events (specular-point reflections), or as a result of nonlinear modulation caused by the long-wave field. The first effect implies that the signal is dominated by few scattering centers and can be described by a discrete scattering model with a fluctuating number of scattering centers. In the latter case, the signal is modeled as a result of a nonstationary modulation process, which can statistically be described by a compound distribution. Both effects can, under the assumption specified previously above, be shown to lead to K_ν -distributed amplitude statistics. We notice that the model proposed in [14] and [16] is also based on compound statistics, where the amplitude probability-density distribution conditioned on the radar cross section $p(A|\sigma_0)$ is the Rayleigh distribution. The amplitude distribution is found from Bayes' theorem by averaging $p(A|\sigma_0)$, with respect to the general distribution for σ_0 . The general distribution for

σ_0 is found starting from the scattering model in (1), and the authors show that for horizontal polarization this leads to the Log-Normal distribution for σ_0 .

C. On the SAR Imaging of a Moving Scatterer with Limited Lifetime

The general expression for the backscattered SAR signal from a rough surface characterized by a complex scattering function γ is given by

$$s_r(t, t_r) = \int \int \gamma(x, y, t) G(Vt - x, y) s_t\left(\frac{2R_0}{c} - t_r\right) \cdot \exp(2jkR_0) dx dy \quad (6)$$

where $t = x/V$ is the azimuth time reference, $t_r = 2R_0/c$ is the range time reference, $G(x, y)$ is the antenna-gain function, $s_t(t_r)$ is the transmitted pulse, V is the platform velocity, R_0 is the range distance, c is the speed of light, and $k = \omega_c/c$ is the wavenumber of the carrier wave. The azimuth time reference t is a discrete sampling of the scattering surface with sampling frequency given by the pulse-repetition-frequency of the radar transmitter. Below we will focus attention to the azimuth resolution, in which case the integral in (6) can be reduced to a one-dimensional (1-D) integral along the x -axis.

The scattering function of a moving scatterer with a limited lifetime is modeled as

$$\gamma(x, y, t) = \gamma_0 \delta\{(x, y) - [(x_0, y_0) + [\mathbf{u}(x, y)t]]\} \cdot \exp(-t^2/2\tau_0^2) \quad (7)$$

where (x_0, y_0) is the initial position, \mathbf{u} is the velocity, and τ_0 is a measure of the lifetime of the scatterer. The velocity \mathbf{u} consists of a slant-range component u_r and an azimuth component u_x . Inserting this scattering function together with a Gaussian antenna pattern into (6), we can find an analytical expression for the azimuth compressed signal [23]. We will emphasize two important results that come out of this calculation.

- 1) The range component of the scatterer velocity will cause a dislocation in the azimuth direction that is given by $(u_r/V)R_0$. This effect is often referred to as the *train-off-the-track* effect in SAR images.
- 2) The spatial resolution in the azimuth direction will be given by

$$\rho_x = \frac{R_0}{2k\tau_0 V}. \quad (8)$$

Hence, when the lifetime of the scatterer τ_0 is less than the integration time of the SAR, this parameter will determine the resolution in the azimuth direction.

In addition, if the scatterer has acceleration, the change in radial velocity according to [2] will cause an additional smearing in the image, with the mean-squared width given by

$$\delta x^2 = \frac{1}{3} \left(\frac{R_0}{V} \dot{u}_r \frac{T}{2} \right)^2 \quad (9)$$

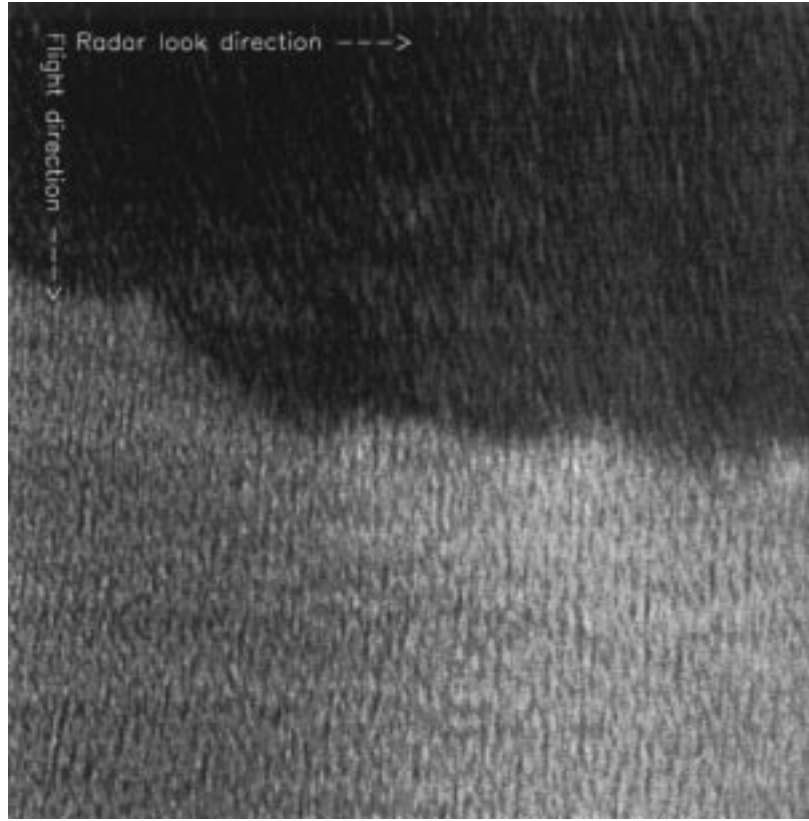


Fig. 1. C-band SAR image of the atmospheric front (March 20, 1988, Pass 2).

where \dot{u}_r is the radial acceleration of the scatterer. The expression given in (9) represents a boxcar averaging over the SAR integration time T .

When imaging a continuous ocean surface, the radial velocity component will continuously vary according to the dynamical laws of the waves, resulting in nonhomogeneous azimuth displacements. This introduces a modulation in the SAR image, which in the literature is referred to as *velocity bunching*. For a known wave spectrum, the velocity-induced modulation can be calculated by using the nonlinear Hasselmann transform (see e.g., [4], [24], and [25]), and an estimate of the smearing caused by velocity bunching can be obtained.

The total acceleration contribution to the smearing can be calculated by averaging (9) over the long-wave ensemble [2], yielding a mean-squared smearing of

$$\sigma_a^2 = g^2 \frac{R^2 T^2}{12 V^2} \int_{-\pi}^{\pi} \int_0^{k_l} k^3 \left(\cos^2 \theta + \frac{k_y^2}{k^2} \sin^2 \theta \right) \cdot \Phi(k, \phi) dk d\phi \quad (10)$$

where g is the gravity acceleration, k_l specifies the limit of the contributing long-wave region, ϕ is the propagation direction of the waves, and θ is the incidence angle. The terms in brackets arise from the projection of vertical and horizontal acceleration components onto the slant-range direction. The effect of this smearing is usually modeled as a low-pass filter of the form

$$F_x(k_x) = \exp \left(-\frac{k_x^2}{2\sigma_{k_x}^2} \right) \quad (11)$$

where $\sigma_{k_x} = 1/\sigma_a$. In [26], it was shown that the effects of orbital acceleration and finite scene-coherence time can in fact be incorporated into the nonlinear Hasselmann transform through the use of an additional cutoff function applied directly to the results of the nondispersive theory.

III. DATA DESCRIPTION AND ANALYZING METHODS

In some of the SAR-data collected on March 20th during the NORCSEX'88 experiment, the presence of a significant atmospheric front was observed (see Fig. 1). This front was imaged by an airborne C-band SAR from a height of approximately 6000 m, overflown in two almost opposite directions. Since the data sets were collected under several imaging geometries and meteorological conditions, they are well suited for studies of the SAR imaging mechanism and the statistical properties of microwave echoes.

1) *SAR System*: The NORCSEX'88 SAR data that are discussed here were collected by the Canadian CV580 SAR system operated in the so-called *nadir-looking mode*. In this mode, the width of the swath is 22 km, covering incidence angles ranging from nadir to about 74° . When multilook images are generated, the spatial resolution is 7×4 m in azimuth and slant-range direction, respectively. The system adds the amplitudes of the subaperture images. Hence, the value of pixel ij , A_{ij} , is then

$$A_{ij} = \sum_{k=1}^7 a_{ij}^{(k)} \quad (12)$$

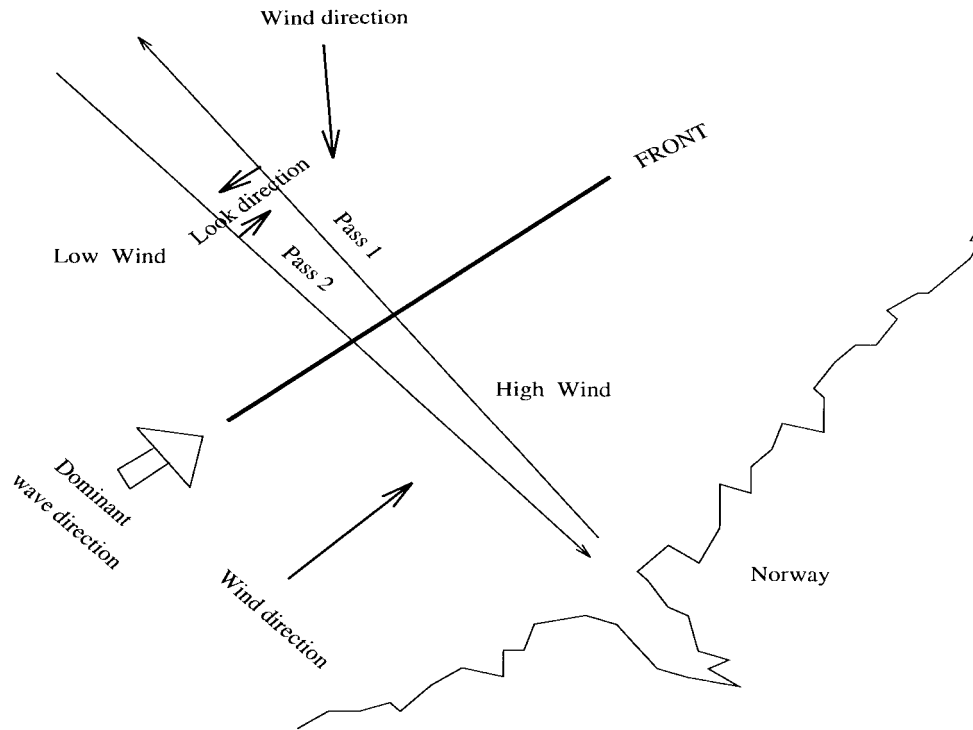


Fig. 2. Map summarizing the meteorological and imaging conditions on March 20, 1988.

where $a_{ij}^{(k)}$ is the envelope signal of subaperture k defined through

$$s_{ij}^{(k)} = a_{ij}^{(k)} \exp [j\phi_{ij}^{(k)}] \quad (13)$$

$s_{ij}^{(k)}$ is the returned complex-envelope signal of subaperture k at pixel ij . The subapertures of the Canadian SAR System have a small overlap, reducing the effective number of independent looks from seven to about six.

2) *Meteorological and Imaging Conditions:* Fig. 1 discloses an abrupt change in the background intensity, which is almost parallel to the range direction. From *in-situ* measurements taken by buoys and an oil rig, this phenomenon has been identified as an atmospheric front. The dark area corresponds to the low-wind side, where the average backscatter cross section was small, and the brighter area is the high-wind side of the front. The *in-situ* measurements revealed that the wind had a dramatic change in direction as well as in speed across the front. On the high-wind side, the wind speed was approximately 12 m/s, whereas on the low-wind side, the speed was 6 m/s. The wind direction changed from southwest on the high-wind side to north-northwest on the low-wind side. There was however no change in the wave direction across the front. The dominant wave direction was from southwest.

In the high-wind area of *Pass 1*, there was an up-wind/up-wave imaging condition, and in the low-wind area, there was a down-wind/up-wave situation. In *Pass 2*, the radar was looking up-wind/down-wave on the low-wind side and down-wind/down-wave on the high-wind side. The imaging and meteorological conditions are summarized in Fig. 2. Figs. 3 and 4 show the SAR image spectra for the various regions. It

TABLE I
INCIDENCE ANGLES AND ROV'S RATIOS FOR THE SELECTED AREAS. THE ACTUAL FLIGHT HEIGHT AND SPEED WERE 6126 m AND 126 m/s, RESPECTIVELY

θ	31.5	46.2	56.0	62.0	66.1	69.1	71.5	72.3
ROV	54.5	67.2	83.1	99.0	114.8	130.7	146.6	153.0

is noted from Fig. 3 that for *Pass 1* the dominant waves are imaged propagating along the range direction and the SAR image spectrum had no significant change across the front. The SAR image spectrum on the high-wind side of *Pass 2* is noted to have a larger azimuth component, and the spectral peak is rotated relative to the range direction across the front.

3) *Analyzing Methods:* To study to which extent the SAR data in these scenes conform to Gaussian or non-Gaussian statistics and to what degree the statistics depend on the imaging and meteorological conditions, we did the following analysis. In each of the four cases, i.e., i) *Pass 1*, low wind, ii) *Pass 1*, high wind, iii) *Pass 2*, low wind, and iv) *Pass 2*, high wind, we selected areas corresponding to eight different incidence angles, and within each area, we calculated the pixel histogram. Each area was 1024×256 pixels in azimuth and range, respectively. For each case, four areas with the same incidence angle were examined. Table I gives the incidence angles and corresponding range-to-velocity ratio (ROV) that were selected. The angle refers to the center of each segment.

The histograms were compared to those density functions obtained by sequentially convolving six probability-density functions of the Rayleigh and K_ν -distribution, respectively, with optimally tuned parameters. The convolution operation is necessary to account for the multilook summation involved

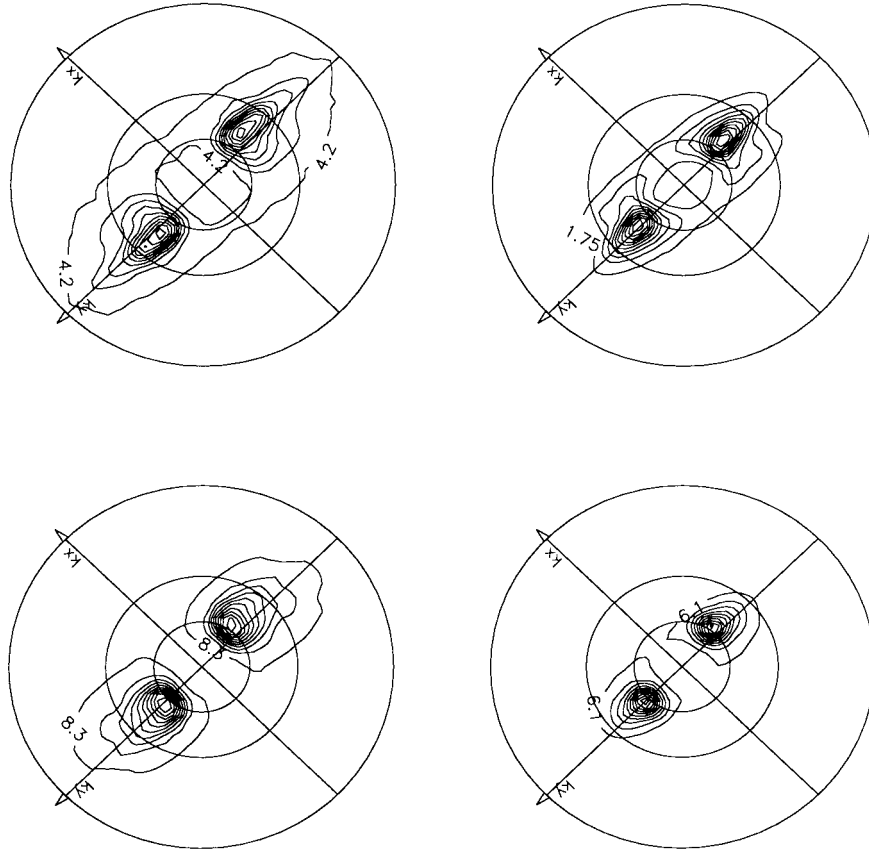


Fig. 3. SAR image spectra from Pass 1 calculated at ROV equal to 60 and 130. North is upwards, k_y is range direction, and k_x is azimuth direction. The circles mark the 75-, 150-, and 300-m wavelengths. Top: High-wind side. Bottom: Low-wind side.

in the SAR image generation. It is assumed that the six subaperture images are uncorrelated. This convolution operation complicates the use of a standard parameter estimation procedure, like, for instance, the maximum likelihood method, for estimating the parameters of the two statistical models. On the other hand, since we are using these models merely to decide if the data are Gaussian or non-Gaussian, we have chosen to apply the minimum L1-norm of the deviation between the histogram and the model density function as an optimization criterion for finding the best model parameters. Hence, let $h_k(A)$ denote the pixel histogram of segment k , and let $p_i(A, \mathbf{c})$ define the resultant density function after the convolution operation. The index i refers to the model function, i.e., either to the Rayleigh or to the K_ν density function, and \mathbf{c} is a parameter vector, which in the Rayleigh case is $\mathbf{c} = [\sigma]$ and in the K_ν case is $\mathbf{c} = [\nu, b]^t$ [see (4) and (5)]. The parameters were selected by searching the parameter space for those values that minimized the total deviation δ_i defined by

$$\delta_i = \int |h_k(A) - p_i(A, \mathbf{c})| dA. \quad (14)$$

This procedure was found to be computationally feasible and to work well in practice. In the remainder, $\delta_{i, \min}$ will be used as a measure of the total discrepancy between the histogram and the statistical model, where again i refers to the Rayleigh or K_ν -distribution.

IV. RESULTS

In this section, we present the results of the analysis of the SAR data.

A. Analysis of the NORCSEX'88 Airborne SAR Data

1) *Dependency of Incidence Angle*: Figs. 5 and 6 show two examples of how the image histograms compare to the Rayleigh and K_ν -models. The histograms show the pixel-value distributions on the high-wind side of Pass 1 at incidence angles 31.5° (Fig. 5) and 69.1° (Fig. 6). We note that there is much less variance in the first data set than in the second. We also immediately observe that the histogram in Fig. 5 has a much larger deviation from the best-fitted Rayleigh model than the best K_ν -model. In this case, the optimal model order for the K_ν -model was calculated to $\nu = 1.25$, resulting in a minimum total deviation $\nabla_{K, \min} = 0.092$. The corresponding minimum total deviation for the Rayleigh-model was $\nabla_{\text{Ray}, \min} = 0.316$.

The histogram in Fig. 6 can be well described by both models. The optimal K_ν -model order of the histogram in Fig. 6 was $\nu = 7.25$, and the calculated deviations were $\nabla_{K, \min} = 0.025$, and $\nabla_{\text{Ray}, \min} = 0.076$, respectively. For the low incidence angle case, the histogram has too much weight in the tail to be well described by the Rayleigh-model. The fit to the K_ν -model is much better, but not perfect. In the high incidence angle case, both models fit well to the data, however, the K_ν -model matches the data best. Figs. 7–9

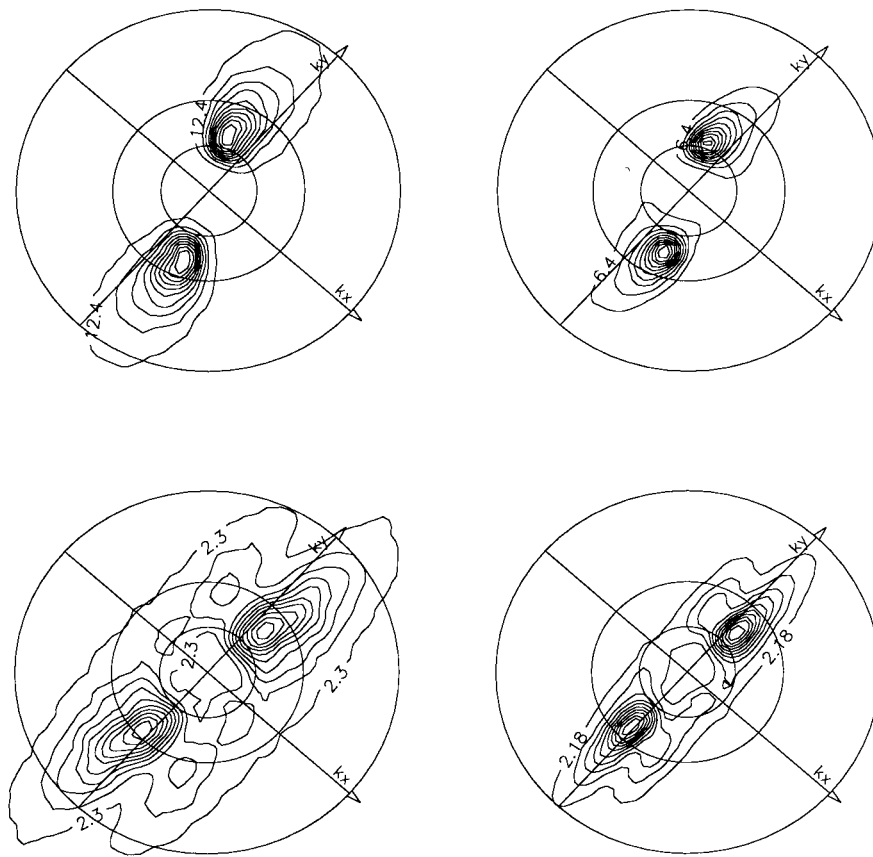


Fig. 4. SAR image spectra from Pass 2 calculated at ROV equal to 60 and 130. Top: Low-wind side. Bottom: High-wind side.

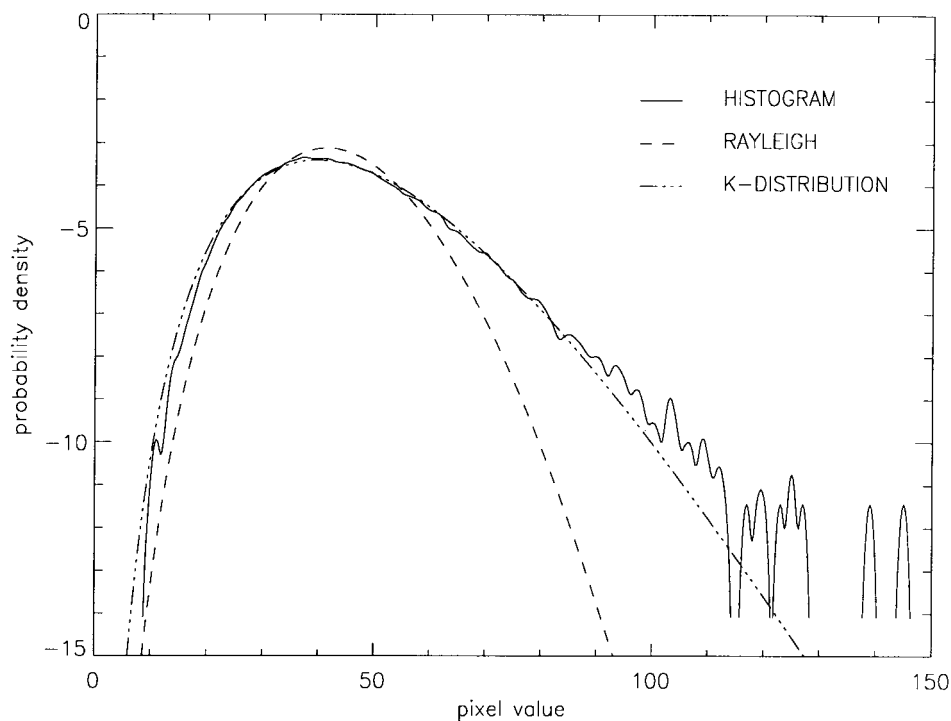


Fig. 5. SAR image pixel value histogram calculated at incidence angle 31.5° , semilogarithmic plot (Pass 1).

summarize the results of the dependency of the histogram on incidence angle for the four imaging conditions encountered in the March 20th data. Fig. 7 shows the optimal K_ν -model order as a function of the ROV ratio. (The correspondence between

ROV ratio and incidence angle is found in Table I.) The error flags represent the standard deviation based on the four calculations in each case. The total deviations from the best-fitted K_ν -model and Rayleigh model are plotted in Figs. 8 and

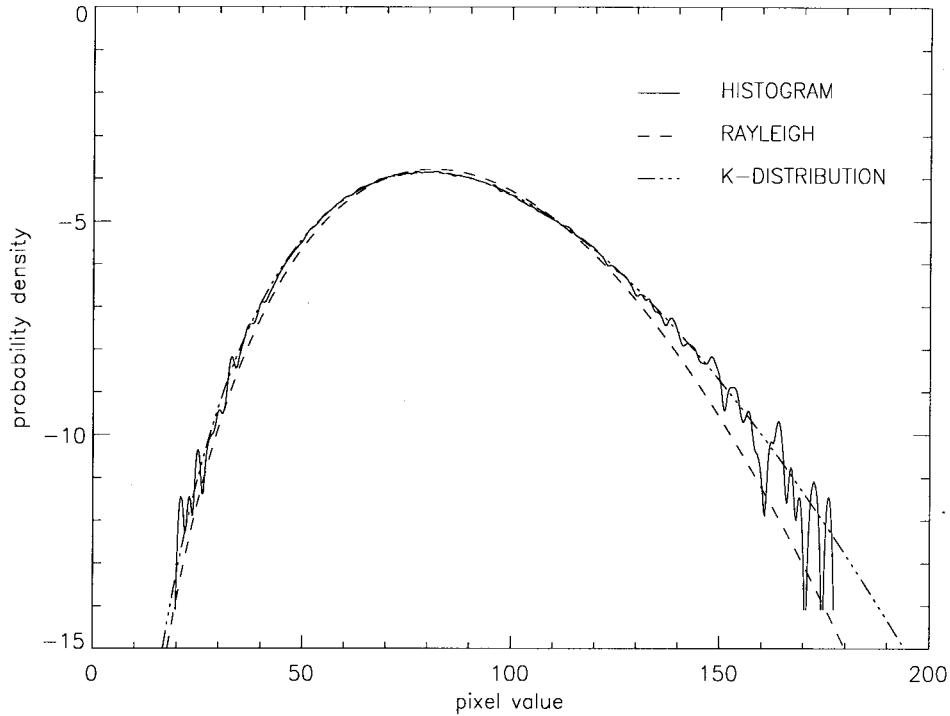


Fig. 6. SAR image pixel value histogram calculated at incidence angle 69.1° , semilogarithmic plot (Pass 1).

9, respectively. From these plots we can make the following observations.

- 1) The model order of the best-fitted K_ν -model always increases with incidence angle.
- 2) The deviation from the best-fitted K_ν -model decreases with incidence angle.
- 3) The deviation from the best-fitted Rayleigh model decreases with incidence angle. It is, however, always larger than the deviation from the K_ν -model.

We note that, as the order of the K_ν -model gets large, the K_ν -model approximates the Rayleigh model. In fact, as ν goes to infinity, the two models are the same. We may therefore conclude that, for low incidence angles, the signal statistics deviate significantly from Gaussian statistics. However, deviation from Gaussian statistics are also found for incidence angles as large as 50° .

2) *Dependency of Wind and Waves:* Comparing the filled and unfilled circles in Figs. 7–9, we can make inferences about the influence of the different wind conditions on the high and low-wind side of Pass 1 on the signal statistics. We observe that the general trend is that the optimal K_ν -model order is much larger on the high-wind side than on the low-wind side. This implies (see paragraph above) that the deviation from non-Gaussian statistics is larger on the low-wind side. This observation is indeed in agreement with Fig. 9, where the total deviation from the Rayleigh distribution are found to be larger on the low-wind side. We find the same trend in the Pass 2 data, when we compare the filled and unfilled diamonds in Figs. 7–9. The low-wind side has larger deviation from Gaussian statistics.

Comparing the data from Pass 1 and Pass 2, we find that the data from Pass 2 are best fitted by K_ν -models of lower order

than the data from Pass 1 and that the total deviation from the Rayleigh model generally is larger. The low-wind side data of Pass 2 is indeed extremely badly fitted by Rayleigh models. As can be noted from Fig. 2, in this case, the wind is blowing almost against the waves and the radar is pointing against the wind. On the high-wind side, the radar is looking in the same direction as the dominant waves and the wind.

Comparing the image spectra on the high-wind side of Pass 2 with the corresponding spectra of Pass 1 (see Figs. 3 and 4), we note that the spectra in Pass 2 have been split and that the off-range spectral content is significant. This phenomenon was explained in [27] as a change in the real aperture radar (RAR) modulation transfer function across the atmospheric front. We also note from these spectra that the images have much higher contrast on the low-wind side of the front than on the high-wind side.

3) *Azimuth Smearing:* From the statistical analysis of the data in the preceding sections, we observe that the signals have a rather strong deviation from Gaussian statistics, even at large incidence angles. According to Section II, non-Gaussian signal statistics may be associated with broadband scattering events, which theoretically should cause more azimuth smearing than Gaussian scenes. Pass 1 represents a good case study for examining the relation between the signal statistics and the smearing of the SAR image spectrum because, in this case, the waves are dominantly range traveling and the velocity bunching effect is limited. By fitting the function $\exp[-(k_x^2 \sigma_{k_x}^2 / 2\pi)]$ to averaged azimuth profiles of the SAR image spectra, we define σ_{k_x} as a *smearing indicator*. In Fig. 10, we have shown plots of σ_{k_x} calculated from spectra estimated in the selected areas. It is noted that the low-wind side, which has the greatest deviation from Gaussian statistics, is also smeared the most.

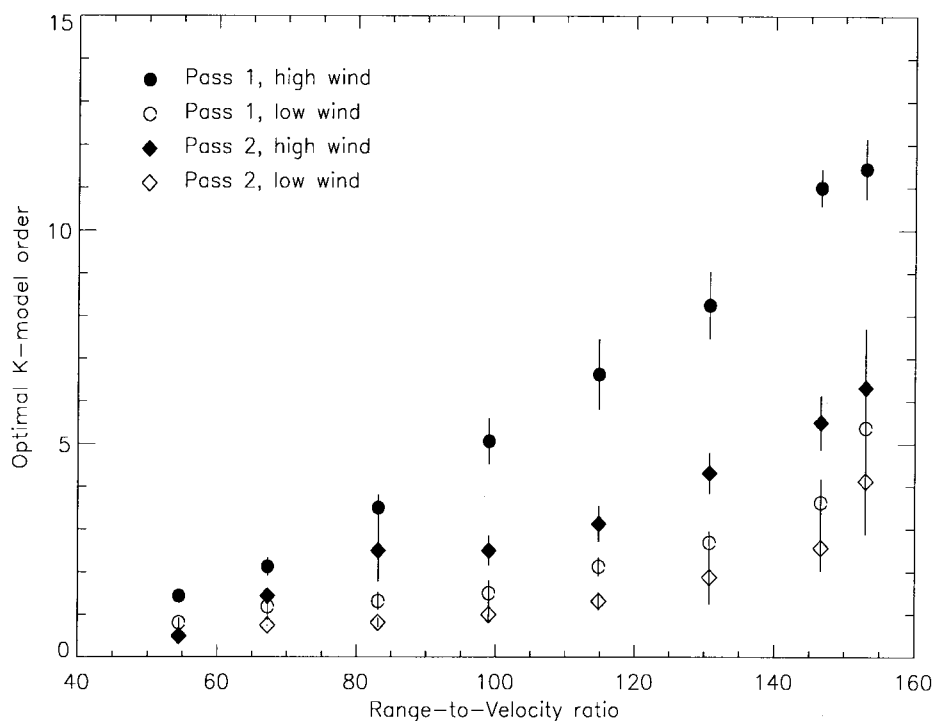


Fig. 7. Calculated optimal K -model order as a function of ROV for the four different SAR imaging conditions.

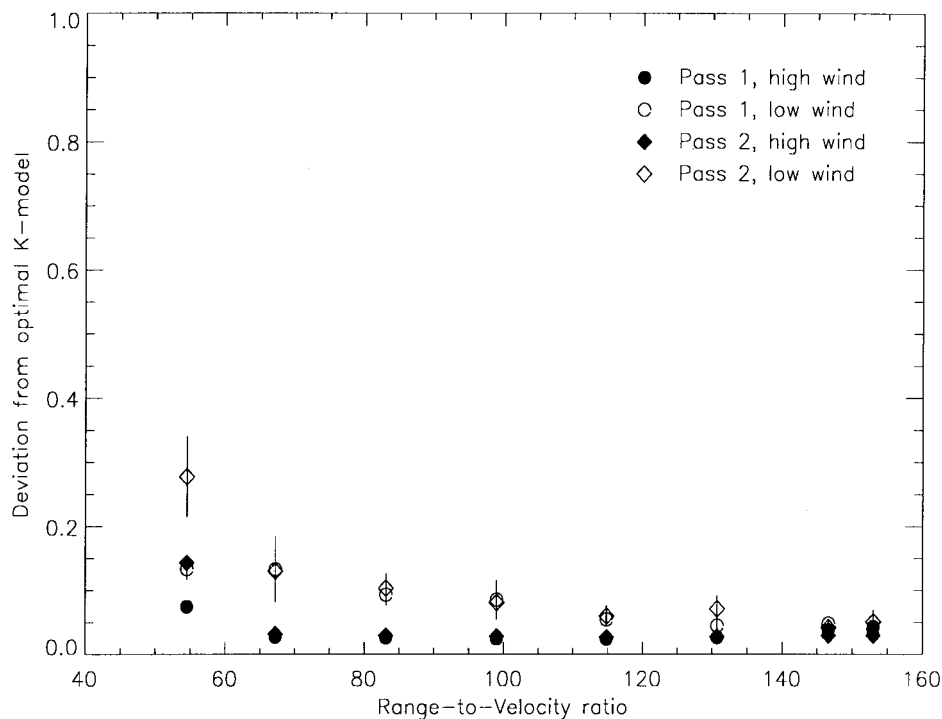


Fig. 8. Calculated total deviation from the optimal K -model as a function of ROV for the four different SAR imaging conditions.

B. Analysis of the NORCSEX'91 ERS-1 SAR Data

The SAR system onboard ERS-1 is a three-look C-band SAR, illuminating the surface of the earth at an incidence angle of 23° . The data we looked at were collected at Haltenbanken, west of Norway; all scenes are from ascending orbits. The waves were mostly coming in from the west, and the wind speed was varying, both in speed and direction (see Table II).

1) *Statistics:* Because of the relatively small incidence angle of the ERS-1 SAR, the probability of specular-point reflections is high, and we expect this to influence on the signal statistics. We have analyzed SAR scenes from orbit 1889, 1975, 2018, and 2061, recorded during the NORCSEX'91 campaign, which cover approximately the same geographic area as the data discussed in the previous section. In Fig. 11,

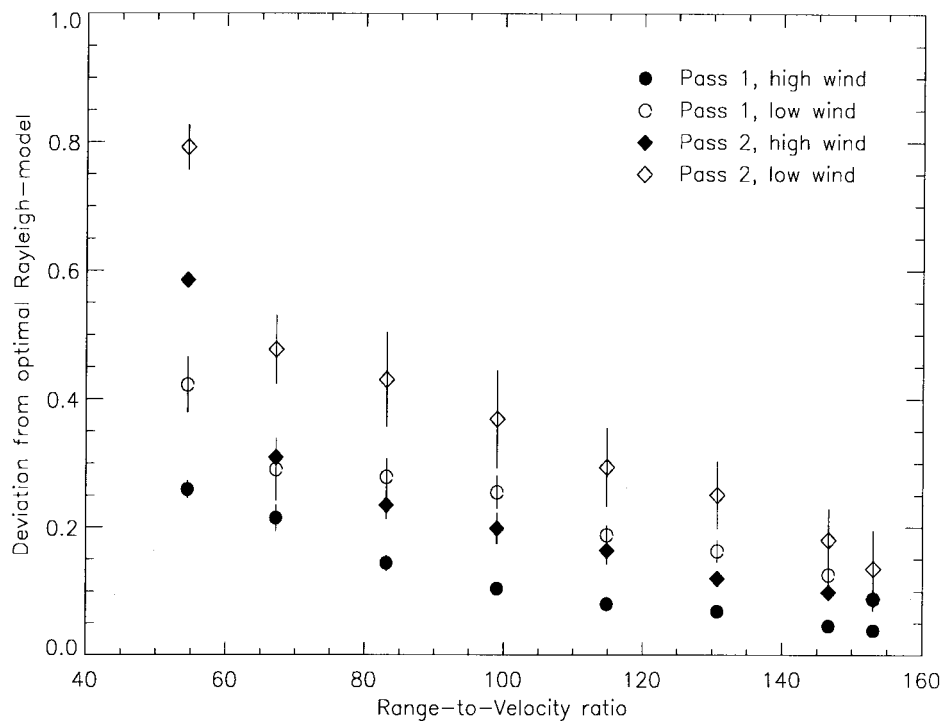


Fig. 9. Calculated total deviation from the optimal Rayleigh-model as a function of ROV for the four different SAR imaging conditions.

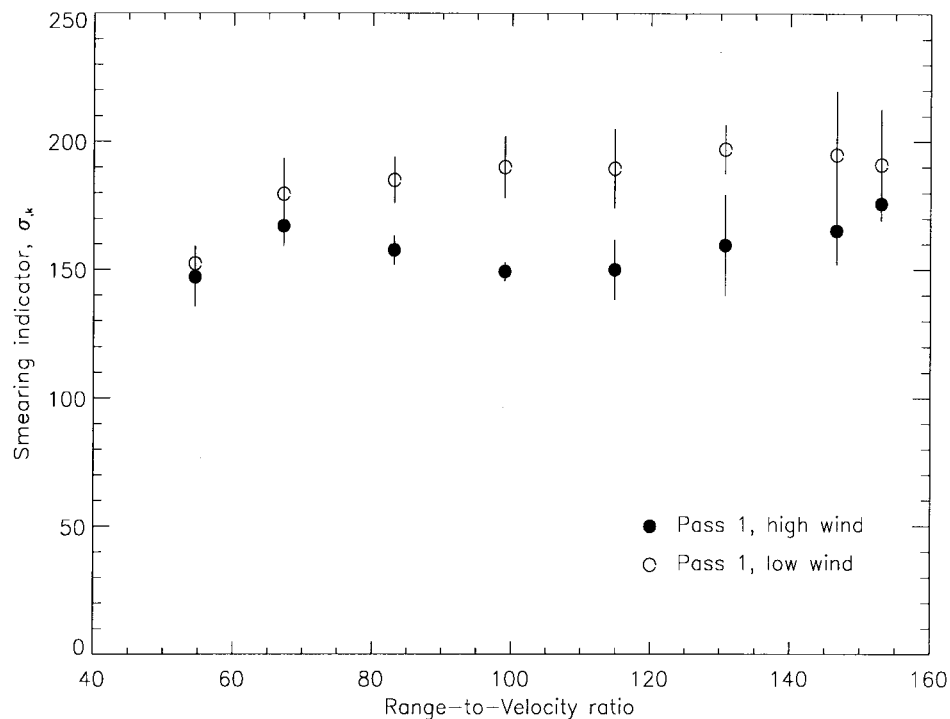


Fig. 10. Estimated azimuth smearing of the SAR image spectra as a function of ROV for Pass 1 data.

we have compared the histogram of one ERS-1 scene (orbit 1889) with the best-fitted K_ν - and Rayleigh models. We observe that the K_ν -model approximates the shape of the histogram much better than the Rayleigh distribution. The model order of the best-fitted K_ν -model was 1.8, which corresponds to a large deviation from Gaussian statistics.

2) *Azimuth Smearing*: We also examined the azimuth smearing of these data. As noted from Section II, there are three effects that all contribute to this degradation of an ocean

SAR scene, namely, *velocity-smearing (velocity bunching)*, *acceleration-smearing*, and *short-coherence-time-smearing*. Our objective was to find out the importance of the last of these effects. In order to do this, we estimated the contributions from the first two effects for the actual sea state by using the procedures described in Section II.

By using a buoy-measured ocean-wave spectrum as input to a numerical simulator of the forward SAR transform, the amount of smearing caused by the velocity of the scatterers

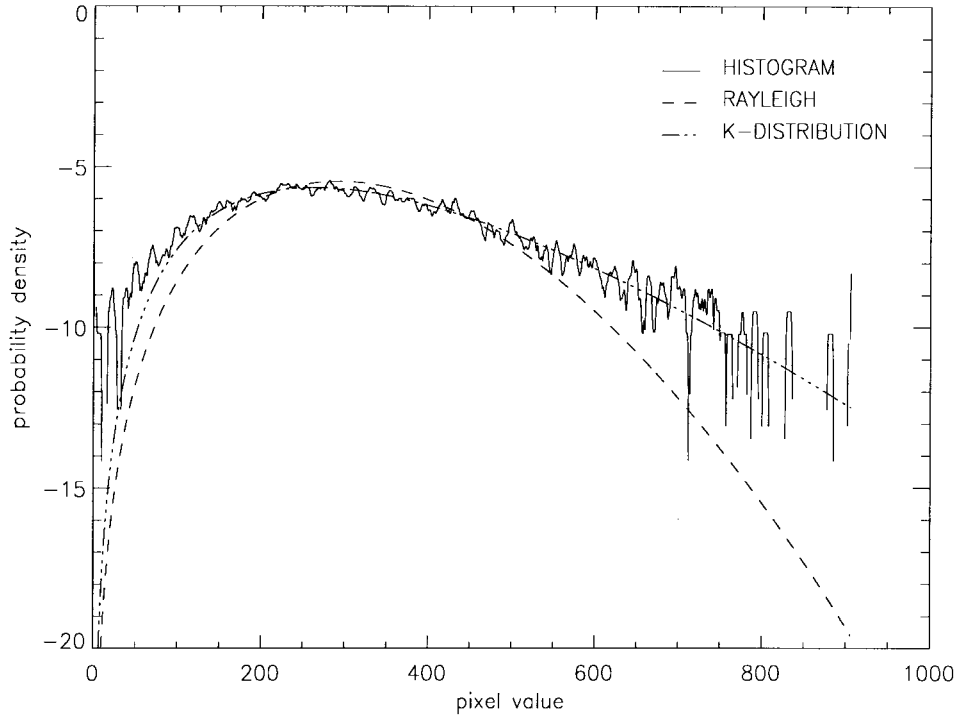


Fig. 11. Pixel value histogram of data from an ERS-1 scene, semilogarithmic plot.

TABLE II
WAVE AND WIND DATA FOR THE ERS-1 SCENES OBTAINED FROM A WAVESCAN BUOY. THE ANGLE IS RELATIVE TO NORTH (MEASURED CLOCKWISE)

Orbit no.	1889	1975	2018	2061
Wave height	3.6 m	2.7 m	2.5 m	2.3 m
Wind speed	1 m/s	9 m/s	13 m/s	14 m/s
Wind direction	308°	267°	34°	222°

TABLE III
ERS-1 ORBIT NO. AND THE CORRESPONDING SCENE COHERENCE TIME (IN s) ESTIMATED FROM THE WIDTH OF THE SMEARING FILTER

Orbit no.	1889	1975	2018	2061
Coherence time	.007	.016	.006	.009

was calculated. As can be noted from the upper part of Fig. 12, this effect alone is not sufficient to account for the amount of smearing the measured spectrum has suffered.

We then included the acceleration smearing as a Gaussian low-pass filter by using (10) and (11). In addition, an extra *subresolution* velocity-smearing filter was added to account for the fact that the numerical simulator-input buoy spectrum has finite resolution. We calculated this smearing by extending the measured buoy spectrum outside the buoy's resolution wavenumber by a $|k|^{-4}$ -spectrum in all directions, keeping the significant wave height constant.

The smearing related to widebanded scatterers was finally included as an additional smearing filter of the form

$$F_r(k_x) = \exp\left(-\frac{k_x^2}{2\sigma_{\tau_0}^2}\right). \quad (15)$$

Assuming that the lifetime of the scatterers within a facet varies from scatterer to scatterer, we used the *Weibull* distribution (e.g., [28]) to describe this variation in τ_0 . Its density function is defined by

$$p(\tau_0) = \frac{a}{\sigma_{\tau_0}} \tau_0^{a-1} \exp\left(-\frac{\tau_0^a}{\sigma_{\tau_0}^a}\right). \quad (16)$$

We note that $a = 1$ corresponds to the exponential and $a = 2$ to the Rayleigh distribution. Using (8) and (16), the average azimuth resolution of a facet then becomes

$$\rho_a = \frac{R_0 \Gamma\left(\frac{a-1}{a}\right)}{2k\sigma_{\tau_0}^{1/a} V} \quad (17)$$

where $\Gamma(\cdot)$ is the gamma function.

In the lower part of Fig. 12, we have incorporated a Gaussian low-pass filter that accounts for the effects of subresolution velocity-smearing, acceleration-smearing, and short-scene-coherence-time-smearing. We set $\sigma_{\tau_0} = 1/\rho_x$ and $a = 2$ in (16). Using (15), we found that the measured spectral widths of the ERS-1 spectra correspond to average scene coherence times on the order of 0.01 s. See Table III.

V. DISCUSSION

The results of the analysis in Section IV-A can be summarized as follows.

- 1) The deviation from Gaussian statistics is dependent on the incidence angle with most significant deviations at low incidence angles.
- 2) The deviation from Gaussian statistics is dependent on the imaging conditions, with larger deviation when the wind is blowing against the waves.

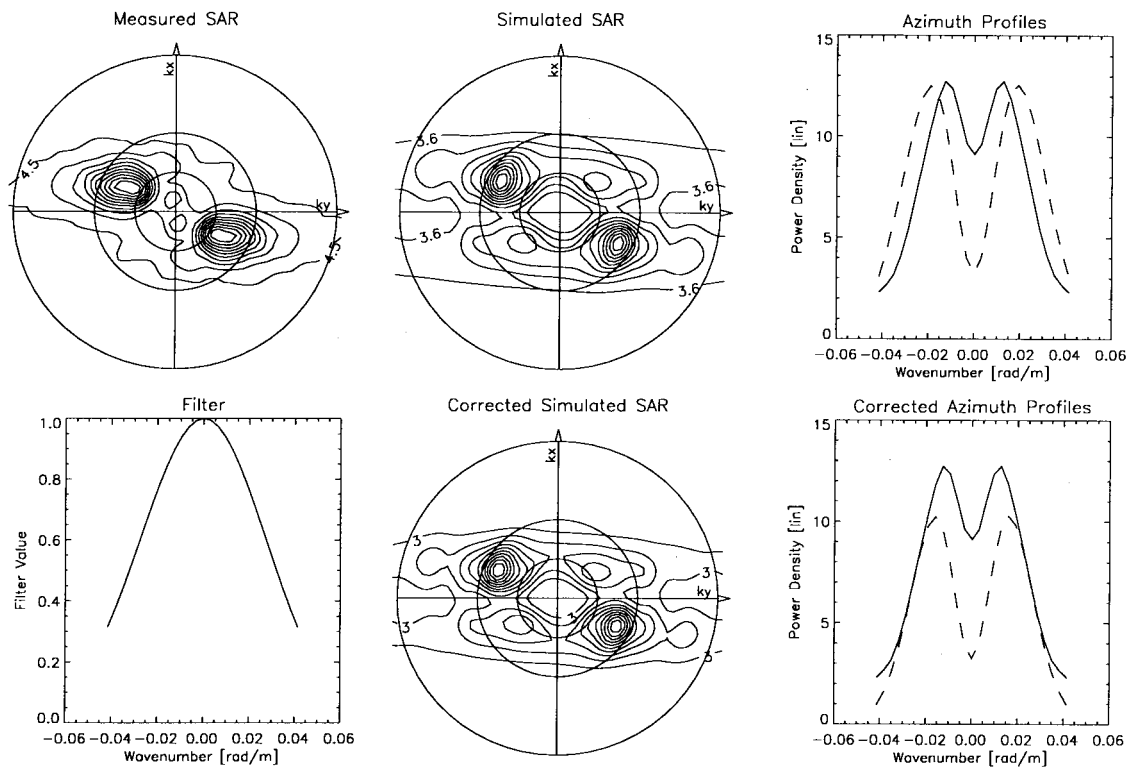


Fig. 12. Top Left: Measured ERS-1 SAR image spectrum. Top Middle: Simulated SAR image spectrum. Top Right: Azimuth profiles of measured (solid line) and simulated (dashed line) spectra. Bottom Left: Shape of Gaussian compression (smearing) filter. Bottom Middle: Compressed simulated spectrum. Bottom Right: Azimuth profiles of measured (solid line) and compressed simulated (dashed line) spectra.

- 3) There is a correlation between the deviation from Gaussian statistics and the azimuth smearing of the SAR images.

We interpret these observations as caused by a combination of the basic scattering mechanism and the modulation of the radar backscatter cross section by the long-wave field. At small incidence angles, the contribution of specular-point reflections to the return signals is generally expected to be significant. Since the nature of these events are strong signals with short coherence time, these effects will render non-Gaussian signal statistics. As the incidence angle increases, Bragg scattering gets more and more dominant and we should expect to get Gaussian signal statistics. We note that the SNR decreases with increasing incidence angle, an effect that is also supposed to change the statistics toward more Gaussian statistics. We have calculated that, for the March 20th scenes, the decrease in SNR corresponds to a factor of two from the lowest to the highest ROV ratios. However, we observe deviations from Gaussian statistics also at incidence angles where specular-point scattering normally is very unlikely. We take these observations as evidence that the modulation mechanisms are also important for the signal statistics. As discussed in Section II-B and [14], non-Rayleigh amplitude statistics can be generated through a compound process, even if the local signal amplitude is Rayleigh distributed. In [14], it was in fact shown that local Rayleigh amplitude statistics were observed for footprints on the order of $1\text{--}3\text{ m}^2$. This supports the theory that modulation of the radar cross section caused by

the long-scale waves represents a significant contribution to the observed non-Gaussian signal statistics. This is also likely to be the case at the small incidence angles.

The difference between the signal statistics across the front may be related to the difference in meteorological conditions, which in turn will have impact on the scattering and modulation mechanisms. On the high-wind side, the wind and the waves have the same direction, while their directions are opposite on the low-wind side. We expect that the latter condition will produce steep wave crests, and as a result, non-Gaussian scattering will occur. Conventional models predict a decreasing coherence time with increasing wind speed, opposite of what we observe. In general, non-Gaussian signals will have shorter coherence time [29], resulting in a wider Doppler spectrum and, consequently, in a stronger azimuth smearing. This hypothesis is consistent with the observed stronger smearing of the images on the low-wind side of the front. The same observation was indeed made in [30] when examining Pass 1 of the March 20th data. They proposed non-Bragg scattering as one of several possible mechanisms for explaining the unexpected increase in smearing on the low-wind side. Our results clearly indicate that this explanation is plausible. However, we would like to emphasize that the difference in meteorological conditions across the front may also be accompanied by a difference in the modulation of the scattering cross section. In fact, in [27] it was shown that the splitting and shifting of the SAR image spectra across the front can be predicted by a proper adjustment of the RAR modulation transfer function. Since the modulation

mechanisms evidently have impact on the signal statistics, these relations should be further investigated.

The analysis of the ERS-1 SAR data also demonstrates that non-Gaussian effects are significant in these data sets, and hence, algorithms for retrieval of geophysical parameters should take this fact into account.

VI. CONCLUSION

In the literature, it is agreed that Bragg scattering is the dominant mechanism for microwave backscatter from the ocean surface at intermediate incidence angles (i.e., 20 and 70°). This mechanism is a coherent process that, in general, involves lots of scattering centers, causing the resulting signals to have Gaussian signal statistics. From the theory of linear systems, it is well known that if the input signal to a linear system has Gaussian statistics, so has the output signal. Accordingly, as long as the surface elevation itself is Gaussian and the modulation mechanisms involved in SAR imaging, (i.e., tilt modulation, hydrodynamical modulation, and velocity bunching), are linear, the signals produced by Bragg scattering should be Gaussian.

For low incidence angles, however, the importance of specular-point reflection will become more significant. Specular-point reflection occurs when the local normal of a surface patch is directed toward the receiver, an event that normally will be more probable at low incidence angles. The echoes produced by this mechanism will typically be strong, widebanded echoes, which conform to non-Gaussian statistics.

In this paper, we have studied the importance non-Gaussian signal statistics in some SAR scenes from the NORCSEX'88 and NORCSEX'91 experiments. At the outset, we have given a brief discussion on microwave scattering from the ocean surface, followed by some theoretical arguments about the statistics of the respective scattering models. It is argued that Bragg scattering, in general, will give signals with Rayleigh-distributed amplitudes, while scattering characterized by few dominant scattering centers will be better described by the K_ν -distribution with low- ν value. In fact, since the K_ν -distribution asymptotically approaches the Rayleigh distribution when ν gets large, we propose to use the ν parameter as a measure of deviation from Gaussian statistics. The data analysis in Section IV shows that when ν becomes larger than six, the two distributions are very close.

The scenes from the NORCSEX'88 represents four different imaging and meteorological conditions. The analysis shows that, at low incidence angles, the deviation from Gaussian statistics is significant in all four cases. We note that, even at incidence angles as high as 50°, this deviation is not negligible. At this incidence angle specular-point reflections are very unlikely, and these observations may be attributed to modulation effects. We find that the deviation from Gaussian statistics is strongly dependent on the imaging conditions. The strongest deviations occur when the wind is blowing against the waves. This is in agreement with the hypothesis that this condition will produce steep waves with high probability of non-Gaussian scattering.

We also find that there is a correlation between the degree of deviation from Gaussian statistics and the azimuth smearing of

the SAR image spectra. This finding supports the interpretation that the deviation is caused by strong widebanded signals, which during the SAR compression process are smeared out in the azimuth direction. Such signals may be due to non-Gaussian scattering events and/or strong, possibly nonlinear, modulation effects.

In Section IV-B, we discussed the statistics of some ERS-1 scenes collected during the NORCSEX'91 campaign. Since the incidence angle of the ERS-1 C-band SAR is only 23°, it is expected that these data will contain significant contribution from specular reflection. Our investigations show that the amplitude of the ERS-1 SAR signals are well described by a K_ν -model with $\nu = 1.8$, implying that there is a significant deviation from Gaussian statistics. We also find, by studying the width of the corresponding SAR spectra, that the amount of smearing that these spectra have been subjected to cannot be explained by the velocity- and acceleration-induced effects alone. By including a smearing filter that accounts for the short coherence time, we are able to match the width of the SAR spectrum. This method also gives an estimate of the average lifetime of the scatterers. The inclusion of this latter effect is considered to be important for the correct retrieval of oceanographic parameters, like significant wave height and wind speed from satellite-borne SAR systems.

ACKNOWLEDGMENT

The authors wish to thank S. Jacobsen, University of Tromsø, for his critical remarks and the anonymous reviewers for their helpful comments and suggestions.

REFERENCES

- [1] W. R. Alpers and C. L. Rufenach, "The effect of orbital motions on synthetic aperture radar imaginary of ocean waves," *IEEE Trans. Antennas Propagat.*, vol. AP-27, pp. 685–690, Sept. 1979.
- [2] K. Hasselmann, R. K. Raney, W. J. Plant, W. Alpers, R. A. Shuchman, D. R. Lyzenga, C. L. Rufenach, and M. J. Tucker, "Theory of synthetic aperture radar ocean imaging: A MARSEN view," *J. Geophys. Res.*, vol. 90, pp. 4659–4686, 1985.
- [3] D. R. Lyzenga, "An analytic representation of synthetic aperture radar image spectrum for ocean waves," *J. Geophys. Res.*, vol. 93, pp. 13 859–13 865, 1988.
- [4] K. Hasselmann and S. Hasselmann, "On the nonlinear mapping of an ocean wave spectrum into a SAR image spectrum and its inversion," *J. Geophys. Res.*, vol. 96, pp. 10 713–10 729, 1991.
- [5] G. Engen and H. Johnsen, "SAR-ocean wave inversion image cross spectra," *IEEE Trans. Geosci. Remote Sensing*, vol. 33, pp. 1047–1056, July 1995.
- [6] G. R. Valenzuela, "Theories for the interaction of electromagnetic and ocean waves—A review," *Boundary Layer Meteorol.*, vol. 13, pp. 61–85, 1978.
- [7] J. O. Jenkins, J. P. Randolph, D. G. Tilley, and C. A. Waters, "The APL image processing laboratory," *APL Tech. Dig.*, vol. 5, pp. 59–78, 1984.
- [8] K. Ouchi and R. A. Cordey, "Statistical analysis of azimuth streaks observed in digitally processed CASSIE imagery of the sea surface," *IEEE Trans. Geosci. Remote Sensing*, vol. 29, pp. 727–735, Sept. 1991.
- [9] D. P. Winebrenner and K. Hasselmann, "Specular point scattering contribution to the mean synthetic aperture radar image of the ocean surface," *J. Geophys. Res.*, vol. 93, pp. 9281–9294, 1988.
- [10] G. V. Trunk and S. F. George, "Detection of target in non-Gaussian sea clutter," *IEEE Trans. Aerosp. Electron. Syst.*, vol. AES-6, pp. 620–628, Sept. 1970.
- [11] E. Jakeman and P. N. Pusey, "A model for non-Rayleigh sea echo," *IEEE Trans. Antennas Propagat.*, vol. AP-24, pp. 806–814, Nov. 1976.
- [12] E. Jakeman, "On the statistics of K-distributed noise," *J. Phys. A: Math. Gen.*, vol. 13, pp. 31–48, 1980.

- [13] E. Jakeman and R. J. A. Tough, "Non-Gaussian models for the statistics of scattered waves," *Ad. Phys.*, vol. 37, pp. 471–529, 1988.
- [14] B. L. Gotwols and D. R. Thompson, "On microwave backscatter distributions," *J. Geophys. Res.*, vol. 99, pp. 9741–9750, 1994.
- [15] J. W. Wright, "A new model for sea clutter," *IEEE Trans. Antennas Propagat.*, vol. AP-16, pp. 217–223, Mar. 1968.
- [16] D. R. Thompson and B. L. Gotwols, "Comparisons of model predictions for radar backscatter amplitude probability density functions with measurements from SAXON," *J. Geophys. Res.*, vol. 99, pp. 9725–9740, 1994.
- [17] D. Holliday, "Resolution of a controversy surrounding the Kirchhoff approach and the small perturbation method in rough surface scattering theory," *IEEE Trans. Antennas Propagat.*, vol. AP-35, pp. 120–122, Jan. 1987.
- [18] D. R. Thompson, "Doppler spectra from the ocean surface with a time-dependent composite model," in *Radar Scattering from Modulated Wind Waves*, G. J. Komen and W. A. Oost, Eds. Norwell, MA: Kluwer, 1989, pp. 27–40.
- [19] D. R. Thompson, B. L. Gotwols, and W. C. Keller, "A comparison of Ku Band Doppler measurements at 20° incidence with predictions from a time-dependent scattering model," *J. Geophys. Res.*, vol. 96, pp. 4947–4955, 1991.
- [20] E. Jakeman and P. N. Pusey, "Significance of K distributions in scattering experiments," *Phys. Rev. Lett.*, vol. 40, pp. 546–550, 1978.
- [21] C. J. Oliver, "Representation of radar sea clutter," *Proc. Inst. Elect. Eng.*, vol. 135, pp. 497–500, 1988.
- [22] K. D. Ward, C. J. Baker, and S. Watts, "Maritime surveillance radar, 1, radar scattering from the ocean surface," *Proc. Inst. Elect. Eng. Part F, Radar Signal Processing*, vol. 137, pp. 551–563, 1990.
- [23] R. O. Harger, *Synthetic Aperture Systems*. New York: Academic, 1970.
- [24] H. E. Krogstad, "A simple derivation of Hasselmann's nonlinear ocean-synthetic aperture radar transformation," *J. Geophys. Res.*, vol. 97, pp. 2421–2425, 1992.
- [25] K. A. Høgda, S. Jacobsen, H. E. Krogstad, and G. Engen, "Azimuth smearing in ocean-synthetic aperture radar image spectra: A study of Hasselmann's closed-form transformation based on Norwegian Continental Shelf Experiment 1988 synthetic aperture radar data," *Radio Sci.*, vol. 28, pp. 501–512, 1993.
- [26] H. E. Krogstad, O. Samset, and P. W. Vachon, "Generalization of the nonlinear ocean-SAR transformation and a simplified inversion algorithm," *Atmos. Ocean*, vol. 31, pp. 81–82, 1994.
- [27] S. Jacobsen and K. A. Høgda, "Estimation of the real aperture radar modulation transfer function directly from synthetic aperture radar ocean wave image spectra without *a priori* knowledge of the ocean wave height spectrum," *J. Geophys. Res.*, vol. 99, pp. 14 291–14 302, 1994.
- [28] P. L. Meyer, *Introductory Probability and Statistical Applications*. Reading, MA: Addison-Wesley, 1970.
- [29] R. K. Raney, "Theory and measure of certain image norms in SAR," *IEEE Trans. Geosci. Remote Sensing*, vol. 23, pp. 343–348, May 1985.
- [30] C. L. Rufenach, R. A. Shuchman, N. P. Malinas, and J. A. Johannessen, "Ocean wave spectral distortion in airborne synthetic aperture radar imagery during the Norwegian Continental Shelf Experiment of 1988," *J. Geophys. Res.*, vol. 96, pp. 10 453–10 466, 1991.



Torbjørn Eltoft (A'93) received the M.S. and Ph.D. degrees from the University of Tromsø, Tromsø, Norway, in 1981 and 1984, respectively.

In 1988, he became an Associate Professor in Applied Physics at the University of Tromsø. Since 1984, he has been interested in remote sensing, with an emphasis on SAR imaging of ocean waves and scattering of microwaves from the ocean surface. His present areas of interest include signal and image processing as well as remote sensing.



Kjell A. Høgda received the M.Sc. degree in applied physics (SAR applications/image processing) in 1988 and the Ph.D. degree in applied physics (SAR ocean wave imaging) in 1993, both from the University of Tromsø, Tromsø, Norway.

In 1988, he joined NORUT Information Technology Ltd., Tromsø, Norway, as a Research Scientist with special interests in SAR and ocean wave imaging. His research interests also include image processing and use of optical satellite instruments for environmental monitoring.